

# CBMC-V3: A CNS-inspired Control Framework Towards Manipulation Agility with SNN

Yanbo Pang, Qingkai Li, Mingguo Zhao

**Abstract**—As robotic arm applications extend beyond industrial settings into service-oriented sectors such as catering, household and retail, existing control algorithms struggle to achieve the agile manipulation required for complex environments with dynamic trajectories, unpredictable interactions, and diverse objects. This paper presents a biomimetic control framework based on Spiking Neural Networks (SNN), inspired by the human Central Nervous System (CNS), to achieve agile control in such environments. The proposed framework features five control modules (cerebral cortex, cerebellum, thalamus, brainstem, and spinal cord), three hierarchical control levels (first-order, second-order, and third-order), and two information pathways (ascending and descending). Each module is fully implemented using SNN. The spinal cord module uses spike encoding and Leaky Integrate-and-Fire (LIF) neurons for feedback control. The brainstem module employs a network of LIF and non-spiking LIF neurons to dynamically adjust spinal cord parameters via reinforcement learning. The thalamus module similarly employs a network of LIF and non-spiking LIF neurons to adjust the cerebellum’s torque outputs via reinforcement learning. The cerebellum module, which provides feedforward gravity compensation torques, uses a recurrent SNN to learn the robotic arm’s dynamics through regression. The framework is validated both in simulation and on real-world robotic arm platform under various loads and trajectories. Results demonstrate that our method outperforms the industrial-grade position control in manipulation agility.

**Index Terms**—Central Nervous System (CNS) inspired, Spiking Neural Network (SNN), Real-time control, Agility, Robotic Arm.

## I. INTRODUCTION

In recent years, robotic arms are increasingly applied in service-oriented sectors such as catering, household and retail. Compared with traditional industrial settings, these scenarios feature more complex environments and diverse tasks while requiring better agility, thereby posing new challenges to control strategies. For instance, a 7-DOF robotic arm can readily cut a circular contour on a workpiece or transport heavy replacement parts, yet it still struggles to perform a task as subtle as peeling an apple, which can be easily accomplished by the human arm. Compared with biological systems, even the most advanced robotic arms today fall short of the agility of human upper limb [1], underscoring the existence of advanced motor control mechanisms in humans that remain underutilized in robotic systems.

In well-modeled environments, control algorithms combining Whole-Body Control (WBC) [2]–[8] and Model Predictive Control (MPC) [9]–[11] can effectively counteract disturbances and achieve strong control performance. Such model-based approaches reflect human capabilities in applying prior

knowledge to solve specific tasks. However, they lack the adaptability inherent to human motor learning. In complex scenarios, variations in the size, mass, or materials of manipulated objects may render the kinematic and dynamic models inaccurate, limiting the effectiveness of these model-based strategies.

With the rapid progress of neural networks, their powerful approximation and learning capabilities have motivated researchers to employ them for adaptive model correction in response to environmental changes. For example, [12] designed feedforward and feedback neural networks to compensate for joint flexibility and friction; [13] employed fuzzy neural networks with adaptive impedance control to handle unknown dynamics and state constraints; [14] proposed a neural-network-based adaptive controller capable of addressing nonlinear dynamics and external disturbances without prior models; [15] integrated genetic algorithm observers with neural networks to compensate for underwater disturbances; [16] investigated the role of hidden-layer size in adaptive control and proposed dynamic adjustment strategies; and [17] applied radial basis function networks with dynamic surface control for robust dual-arm coordination. Despite these progression, they rely on artificial neural networks (ANN), which inherently disregard the temporal-spatial characteristics of motion, focusing only on instantaneous control. Furthermore, they remain constrained by robotic dynamics models, with network structures and training methods often tailored to specific problems and tightly coupled to complex mathematical formulations, thereby limiting generalizability.

Recently, spiking neural networks (SNN) combined with brain-inspired architectures have emerged as promising alternatives. By emulating biological neurons, SNNs process and store information through spike trains and membrane potential dynamics, offering advantages in computational speed, energy efficiency, information dimension, and biological plausibility, making them well-suited for robotic control [18]. For instance, [19] developed a cerebellum-inspired SNN trained via spike-timing-dependent plasticity (STDP) to learn manipulator dynamics for torque control; [20] extended this model to human–robot collaboration scenarios, demonstrating robustness under unknown disturbances; [21] further established resilience to control delays, highlighting potential in teleoperation and cloud robotics; [22] refines this framework to enable robotic arms to dynamically adjust compliance. However, these methods suffer from structural complexity, computational cost, hyperparameter sensitivity, and limited interpretability, as they focus narrowly on cerebellar functionality while neglecting the integrative role of the broader central nervous system (CNS), which coordinates control through

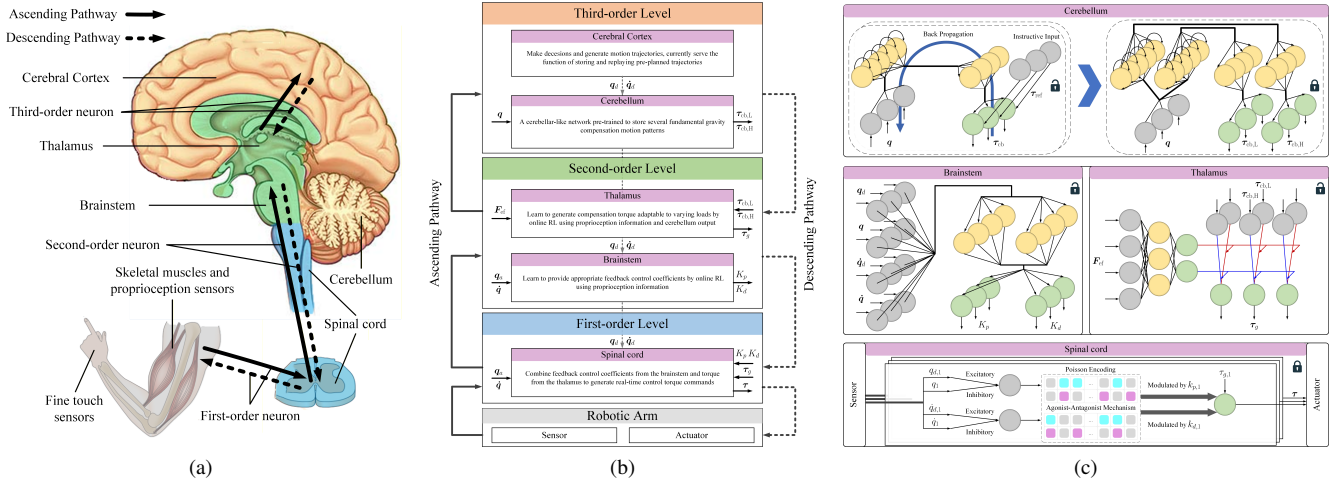


Fig. 1. Overview of the human CNS and the proposed framework structure. (a) Human CNS relating to motion control. Sensory information and motor commands are transmitted through three orders of neurons along ascending and descending pathways. Sensory signals travel from peripheral receptors to the spinal cord, brainstem, and ultimately the cerebellum and cerebral cortex, while motor commands descend from the cerebral cortex and cerebellum through the thalamus and spinal cord to the muscles. The spinal cord can independently generate reflexive responses via reflex arcs, enabling rapid reactions to stimuli [27]. The brainstem contributes to movement termination, reorientation, and coordination with the spinal cord [28], [29]. The thalamus functions as a hub for motor coordination, multimodal perception, and sensorimotor integration [23], [27]. The cerebellum regulates body movements, balance, and posture by integrating sensory inputs and refining motor commands [27]. The cerebral cortex generates decisions and motion trajectories. (b) Schematic diagram of our proposed framework, featuring five modules, three control levels and two pathways as mentioned in (a). (c) Neural network design of each module, utilizing three types of spiking neurons: input fiber (grey), LIF neuron (yellow) and non-spiking LIF neuron (green).

interactions among several neural areas [23].

Inspired by this systemic perspective of the CNS, [24] proposed the CBMC framework, incorporating modules such as the cortex, cerebellum, and spinal cord. Yet its computational inefficiency restricted real-time applicability. Building on this, [25] introduced a hierarchical control architecture deployable on neuromorphic hardware, though its lack of neural networks in some modules compromised accuracy.

Despite these advances, current brain-inspired algorithms have yet to demonstrate agile performance comparable to that of humans. As defined in [26], agility is a capability characterized by rapid and efficient transitions between diverse motion patterns, with precision and speed as its key attributes. In this work, we propose CBMC-V3, a fully SNN-based brain-inspired control framework designed to achieve agile robotic arm control. The key contributions are fourfold: (1) Proposing a CNS-inspired control framework leveraging hierarchical modularity; (2) Designing a fully SNN-based implementation; (3) Validating the framework and module design in simulation experiments; (4) Deploying the algorithm on a robotic platform, demonstrating agility.

The remainder of this paper is organized as follows: Section II introduces the framework structure; Section III details the SNN-based implementations of individual modules; Section IV presents simulation analyses; Section V conducts experiments on a robotic arm platform, and Section VI concludes the study.

## II. FRAMEWORK STRUCTURE

Inspired by the motion control mechanism of the human CNS, as illustrated in Fig.1a, the structure of our proposed framework CBMC-V3 is shown in Fig.1b. This framework consists of three fundamental components: (1) five functional

modules, namely the cerebral cortex module, cerebellum module, thalamus module, brainstem module, and spinal cord module; (2) three hierarchical control levels, namely the first-order, second-order, and third-order level; (3) two information pathways, the ascending and descending pathway. In the following sub-sections, we will introduce each of these components in detail and explain how the framework integrates functional modules, control loops, and information pathways to accomplish a complete operational cycle.

### A. Module function

In the human CNS, the spinal cord can generate reflexive actions independently via reflex arcs, enabling rapid responses to sensory stimuli without cortical input [27]. Inspired by this mechanism, the spinal cord module in our framework implements a PD-like feedback control function, producing torque commands at real-time control frequencies, i.e.,

$$\tau_{fb}(\dot{q}_d, q_d, \dot{q}, q) = \mathbf{K}_V(\dot{q}_d, q_d, \dot{q}, q)(\dot{q}_d - \dot{q}) + \mathbf{K}_P(\dot{q}_d, q_d, \dot{q}, q)(q_d - q) \quad (1)$$

The brainstem has been shown to contain pathways involved in movement termination and reorientation, and to interact with the spinal cord to coordinate motor behaviors [28], [29]. Motivated by this, the brainstem module in our framework dynamically adjusts the PD gains for each joint based on trajectory information, providing the spinal cord module with time-varying proportional and derivative coefficients, i.e.,

$$\mathbf{K}_V(\dot{q}_d, q_d, \dot{q}, q) = \text{diag}(k_{v,1}, k_{v,2}, \dots, k_{v,n}) \quad (2)$$

$$\mathbf{K}_P(\dot{q}_d, q_d, \dot{q}, q) = \text{diag}(k_{p,1}, k_{p,2}, \dots, k_{p,n}) \quad (3)$$

By integrating spinal feedback control with brainstem-driven adaptive gain modulation, the framework circumvents the

complexity of manipulator dynamics while compensating for structured uncertainties through learning.

The gravity compensation torque of a robotic manipulator, denoted as  $\boldsymbol{\tau}_g(\mathbf{q})$ , is a feedforward torque designed to counteract the gravitational forces acting on the manipulator itself. It plays a crucial role in ensuring the smoothness and stability of motion. In human motor control, the cerebellum is primarily responsible for coordinating and regulating body movements, ensuring muscle and postural balance. It integrates sensory inputs, such as muscle tension and joint position, and adjusts the magnitude and direction of motor commands to achieve precise and fluid motion [27]. Analogously, gravity compensation in robotic manipulators serves a function comparable to that of the cerebellum, and thus the cerebellar module in our framework is tasked with providing this compensation. Furthermore, we note that during human arm manipulation, accurate models of dynamics are not strictly required. Instead, the brain relies on stored motor patterns to cope with different loading conditions. For instance, when grasping an object, we estimate its weight based on prior experience and adjust the exerted force accordingly. Such experiential knowledge is typically not acquired on site during execution, but rather accumulated over time through long-term daily interactions. Inspired by this biological mechanism, the proposed framework equips the cerebellum module with the ability to pre-learn multiple gravity compensation ‘patterns’ corresponding to different load masses. These patterns can then be retrieved and combined to generate an  $n \times m$  set of compensation torques,

$$\begin{aligned} \mathbf{T}_{\text{cb}}(\mathbf{q}) &= (\boldsymbol{\tau}_{\text{cb},1}(\mathbf{q}), \boldsymbol{\tau}_{\text{cb},2}(\mathbf{q}), \dots, \boldsymbol{\tau}_{\text{cb},m}(\mathbf{q})) \\ &= \begin{pmatrix} \tau_{\text{cb},11} & \cdots & \tau_{\text{cb},1m} \\ \vdots & \ddots & \vdots \\ \tau_{\text{cb},n1} & \cdots & \tau_{\text{cb},nm} \end{pmatrix} \end{aligned} \quad (4)$$

as a function of joint positions, where  $\tau_{\text{cb},ji}(\mathbf{q}), j = 1, \dots, n, i = 1, \dots, m$ , denotes the torque provided for the  $j$ -th joint under the  $i$ -th compensation pattern.

Although suitable motor patterns can often be selected based on prior experience, in certain cases, such selections may be inaccurate due to factors such as visual deception. For instance, the mass of an opaque box cannot be reliably estimated visually, which may lead to insufficient force to move the load or, conversely, an excessive initial force causing large errors. Nevertheless, humans can quickly adjust their motor output upon physically contacting the object, using sensory feedback to correct their movement patterns. This phenomenon is closely associated with the function of the thalamus, which serves as a central hub for motor coordination and plays a critical role in multimodal perception and sensorimotor integration [23], [27]. Analogously, a robotic arm can ‘perceive’ the load weight via force sensors installed at the end-effector. The thalamus module, similar to humans, uses the sensed load information to dynamically weight and integrate the torque contributions provided by the cerebellar module,

generating an actual gravity compensation torque, i.e.,

$$\begin{aligned} \boldsymbol{\tau}_g(\mathbf{q}, \mathbf{F}_{\text{ef}}) &= \mathbf{T}_{\text{cb}}(\mathbf{q}) \cdot \boldsymbol{w}(\mathbf{F}_{\text{ef}}) \\ &= \begin{pmatrix} \tau_{g,1} \\ \vdots \\ \tau_{g,n} \end{pmatrix} = \begin{pmatrix} w_1 \tau_{\text{cb},11} + \cdots + w_m \tau_{\text{cb},1m} \\ \vdots \\ w_1 \tau_{\text{cb},n1} + \cdots + w_m \tau_{\text{cb},nm} \end{pmatrix} \end{aligned} \quad (5)$$

where  $\mathbf{F}_{\text{ef}}$  denotes the end-effector torque sensor feedback,  $\boldsymbol{w}(\mathbf{F}_{\text{ef}}) = (w_1, w_2, \dots, w_m)^T$  represents the dynamically learned weight coefficients of the thalamus module, and  $\tau_{g,1}, \dots, \tau_{g,n}$  are the resulting gravity compensation torques. By combining the prior knowledge stored in the cerebellum module with the adaptive weighting capability of the thalamus module, the framework effectively addresses the unknown dynamics of the manipulator’s end-effector load.

The resulting torque is then summed with the feedback torque generated by the spinal cord module and applied as joint-level control commands to the actuators, i.e.,

$$\boldsymbol{\tau} = \boldsymbol{\tau}_{\text{fb}}(\dot{\mathbf{q}}_d, \mathbf{q}_d, \dot{\mathbf{q}}, \mathbf{q}) + \boldsymbol{\tau}_g(\mathbf{q}, \mathbf{F}_{\text{ef}}) = (\tau_1, \dots, \tau_n)^T \quad (6)$$

where  $\boldsymbol{\tau}_{\text{fb}}(\dot{\mathbf{q}}_d, \mathbf{q}_d, \dot{\mathbf{q}}, \mathbf{q})$  is produced by the spinal cord and brainstem module,  $\boldsymbol{\tau}_g(\mathbf{q}, \mathbf{F}_{\text{ef}})$  is produced by the cerebellum and thalamus module, and  $(\tau_1, \dots, \tau_n)^T$  represents the joint torques delivered to the actuators.

In conclusion, the function of each module can be summarized as follows:

- The cerebral cortex module makes decisions and generates motion trajectories. In this research, it stores and replays pre-planned trajectories.
- The cerebellum module is a cerebellar-like network pre-trained to store several fundamental gravity compensation motion patterns.
- The thalamus module learns to generate compensation torque adaptable to varying loads by online RL using proprioception information and the cerebellum module output.
- The brainstem module learns to provide appropriate feedback control coefficients by online RL using proprioception information.
- The spinal cord module combines feedback control coefficients from the brainstem and torque from the thalamus module to generate real-time control torque commands.

### B. Hierarchical control level

Clearly, different neural regions in the central nervous system operate hierarchically during motion control, with each level specializing in particular tasks while communicating and cooperating through neural pathways. This hierarchical organization enables organisms to execute a wide range of motion tasks flexibly and stably across varying environments. Physiological studies indicate that the multilevel transmission of neural signals is a key component of this hierarchy. Proprioceptive information is conveyed from sensory receptors to the brain via a three-order neuronal pathway [27], [30], as illustrated in Fig. 1a. First-order neurons receive impulses from the skin and muscles and transmit them to the spinal cord. Some of this information is processed locally in the spinal

cord and then relayed back to the muscles through these first-order neurons. The remaining signals pass through second-order neurons, which transmit impulses via the brainstem to the thalamus. Finally, third-order neurons carry these impulses to the cerebral cortex and cerebellum, and are responsible for information exchange between them.

Inspired by this three-order neuronal pathway, the proposed framework implements a corresponding three-level control hierarchy operating at different frequencies:

- First-order level: Comprising the spinal cord module, this level operates at the highest frequency. Its primary function is to generate real-time control torques sent to the robotic arm, ensuring accurate and rapid responses.
- Second-order level: Including the brainstem and thalamus module, this level operates at an intermediate frequency. It serves as a relay between the first-order and third-order levels, performing two main functions: regulating the feedback control coefficients of the first-order level and integrating and filtering the torques provided by the third-order level to supply feedforward torque to the first-order level.
- Third-order level: Comprising the cerebellum and cerebral cortex module, this layer operates at the lowest frequency. Its role is to generate movement trajectories and provide gravity compensation torques based on motion patterns, maintaining movement stability and smoothness.

### C. Information pathway

As illustrated in Fig.1a, the human central nervous system employs ascending and descending pathways for sensory information transmission and motor command execution, respectively. The ascending pathways primarily convey peripheral sensory information to the brain for perception and integration, while the descending pathways transmit motor commands from the brain to the spinal cord and peripheral nerves to control movements. Following this principle, our framework incorporates two analogous information pathways:

- Ascending pathway: Inspired by the dorsal column–medial lemniscal and spinocerebellar tracts [30], this pathway transmits proprioceptive and touch information, namely joint positions, velocities, and end-effector torque. It simulates the process by which muscle receptors relay signals to the CNS for processing and can be regarded as the input process of the framework.
- Descending pathway: Inspired by the corticospinal and reticulospinal tracts [30], this pathway transmits joint torque commands and parameter adjustment signals. It simulates the process by which the CNS delivers motor commands to muscle effectors and can be regarded as the output process of the framework.

### D. A complete operational cycle

To clarify the interplay among modules, levels, and pathways, we illustrate in Fig. 1b a complete working cycle of the proposed framework, showing how sensory inputs are transformed into motor control outputs.

In each cycle, proprioceptive data (actual joint states  $(\dot{q}, q)$  and desired joint states  $(\dot{q}_d, q_d)$ ) are transmitted via first-order neurons to the spinal cord. Part of this input is locally processed to generate feedback torque  $\tau_{fb}$ ; part is relayed via second-order neurons to the brainstem, which adaptively provides PD gains  $(K_P, K_V)$ ; and part is sent via third-order neurons to the cerebellum, which outputs gravity compensation matrix  $T_{cb}$ . These ascending transmissions complete the flow of proprioceptive information from sensors to the modules.

On the descending side,  $T_{cb}$  is conveyed via third-order neurons to the thalamus, where end-effector torque feedback  $F_{ef}$  is integrated to generate a weight vector  $w$ . This vector filters  $T_{cb}$  to produce the effective gravity compensation torque  $\tau_g$ , which is passed via second-order neurons to the spinal cord. There,  $\tau_g$  is combined with  $\tau_{fb}$  to form the final control torque  $\tau$ , which is delivered through first-order neurons to the actuators. Thus, the descending pathway completes motor command transmission from the modules to the joints.

Because information reaches different modules through pathways of varying length, the framework is naturally organized into three control levels. The first-order level involves only spinal processing and yields the shortest latency and highest frequency. The second-order level adds brainstem and thalamic processing, resulting in longer pathways and lower frequency. The third-order level incorporates the cerebellum, producing the longest transmission path and the lowest frequency.

The pseudocode implementation of this framework is provided in Algorithm 1.

## III. MODULE NETWORK DESIGN

Building on the framework introduced in the previous section, this chapter focuses on the implementation of each module using SNNs. The cerebral cortex module, which serves only for trajectory storage and playback, is therefore excluded from the discussion. Since high-performance robotic arms are commonly designed with seven DoF, all implementations in this chapter target a 7-DoF arm. For manipulators with different DoF, the same design principles can be applied by appropriately scaling the neural network architecture of each module.

### A. Spiking neuron

SNN employs spiking neurons as their fundamental computational units. A variety of spiking neuron models have been proposed in the literature, such as the Hodgkin–Huxley model [31] and the Leaky Integrate-and-Fire (LIF) model along with its derivatives [32]. The LIF model is of particular interest here, since it not only captures the dynamic process of membrane potential accumulation and leakage, but also maintains relatively high computational efficiency [33]. Therefore, we will focus on the LIF model.

The input current signal generated by a spike train  $S(t) = \sum_f s(t-t_f)$ ,  $f = 1, 2, \dots$  acting on a neuron can be described as

$$i(t) = \int_0^\infty S(s-t) \exp(-s/\tau_s) ds \quad (7)$$

---

**Algorithm 1** CBMC-V3
 

---

**Require:** joint proprioceptive sensor data  $\dot{\mathbf{q}}, \mathbf{q}$ , planned trajectory data  $\dot{\mathbf{q}}_d, \mathbf{q}_d$ , end-effector torque sensor data  $\mathbf{F}_{ef}$

**Ensure:** joint control torque  $\boldsymbol{\tau}$

```

1: Main thread:
2: initialize first-order, second-order and third-order level control
  cycle  $T_1, T_2, T_3$ 
3: initialize trajectory variables  $\dot{\mathbf{q}}_d, \mathbf{q}_d, \dot{\mathbf{q}}, \mathbf{q}$ 
4: initialize end-effector torque variable  $\mathbf{F}_{ef}$ 
5: initialize control torque variable  $\boldsymbol{\tau}$ 
6: initialize intermediate variables  $\mathbf{K}_V, \mathbf{K}_P, \boldsymbol{\tau}_g, \mathbf{w}, \mathbf{T}_{cb}$ 
7: read trajectory length  $M$ 
8: for  $t = 1$  to  $M$  do
9:   read data from sensors and update  $\dot{\mathbf{q}}_d, \mathbf{q}_d, \dot{\mathbf{q}}, \mathbf{q}, \mathbf{F}_{ef}$ 
10:  if  $t \bmod T_1 == 0$  then
11:    run sub-thread 1
12:  end if
13:  if  $t \bmod T_2 == 0$  then
14:    run sub-thread 2
15:  end if
16:  if  $t \bmod T_3 == 0$  then
17:    run sub-thread 3
18:  end if
19:  send  $\boldsymbol{\tau}$  to actuators
20: end for
21:
22:
23: Sub-thread 1:
24: read  $\dot{\mathbf{q}}_d, \mathbf{q}_d, \dot{\mathbf{q}}, \mathbf{q}, \mathbf{K}_V, \mathbf{K}_P, \boldsymbol{\tau}_g$ 
25: process through the spinal cord module
26: update  $\boldsymbol{\tau}$ 
27:
28: Sub-thread 2:
29: read  $\dot{\mathbf{q}}_d, \mathbf{q}_d, \dot{\mathbf{q}}, \mathbf{q}$ 
30: process through the brainstem module
31: update  $\mathbf{K}_V, \mathbf{K}_P$ 
32:
33: Sub-thread 3:
34: read  $\mathbf{T}_{cb}, \mathbf{F}_{ef}$ 
35: process through the thalamus module
36: update  $\boldsymbol{\tau}_g, \mathbf{w}$ 
37:
38: Sub-thread 4:
39: read  $\mathbf{q}$ 
40: process through the cerebellum module
41: update  $\mathbf{T}_{cb}$ 

```

---

where  $\tau_s$  denotes the synaptic time constant. The membrane potential  $u$  of the neuron evolves according to the following dynamics:

$$\tau_m \frac{du}{dt} = u_{\text{reset}} - u(t) + R \left( i_0(t) + \sum w_j i_j(t) \right) \quad (8)$$

where  $\tau_m = RC$  is the membrane time constant determined by the membrane resistance  $R$  and capacitance  $C$ . Here,  $u_{\text{reset}}$  is the reset potential after firing,  $i_0(t)$  represents the external current driving the neuron,  $i_j(t)$  denotes the input current from the  $j$ -th synapse, and  $w_j$  is the synaptic weight associated with the  $j$ -th synapse. When the membrane potential  $u$  reaches a certain threshold  $u_{\text{fire}}$ , the neuron emits a spike and the potential is reset to  $u_{\text{reset}}$ . Therefore, the operational process of a spiking neuron can be interpreted as follows:

1. When the membrane potential  $u(t)$  exceeds the firing

threshold  $u_{\text{fire}}$ , the neuron emits a spike  $s(t)$ , expressed as

$$s(t) = \Theta(u(t) - u_{\text{fire}}) \quad (9)$$

where

$$\Theta(x) = \begin{cases} 1, & x \geq 0 \\ 0, & x < 0 \end{cases} \quad (10)$$

is the Heaviside step function. Simultaneously, the membrane potential is reset to  $u_{\text{reset}}$ . When the membrane potential  $u(t)$  remains below the threshold  $u_{\text{fire}}$ , no spike is generated.

2. At each time step, the differential equation (8) is updated, where the membrane potential decays by  $|u_{\text{reset}} - u(t)|$  (representing the forgetting effect over time) and increases by  $R(i_0(t) + \sum w_j i_j(t))$  (representing the stimulation effect induced by external inputs).

3. The process then returns to Step 1.

In our framework, we adopt a backpropagation-based training method [34] for SNN. Since the activation function of the neuron in equation (10) is a discontinuous function, directly computing its derivative can lead to network instability. Consequently, various surrogate gradient methods have been proposed [34]. A common approach is to use the original step function  $y = \Theta(a)$  during the forward pass, while replacing its derivative with  $\theta'(a) = \sigma'(a)$  instead of  $\Theta'(a)$  during backpropagation, where  $\sigma(a)$  is referred to as the surrogate activation function. Typically,  $\sigma(a)$  is a smooth and continuous function that resembles the shape of  $\Theta(a)$  while enabling stable gradient computation.

As illustrated in Fig.1c, the framework employs three types of neurons across all modules, represented in gray, yellow, and green. The gray neurons correspond to input fibers, which serve as the data interface for each module via connections to the ascending or descending pathway. The yellow neurons represent LIF neurons, which constitute the core units of SNNs and are responsible for information storage, processing, and learning. The green neurons correspond to non-spiking LIF neurons, implemented by setting the membrane time constant  $\tau_m$  of standard LIF neurons to infinity. Unlike spiking neurons, their output is the continuous membrane potential  $u(t)$  rather than discrete spikes, thereby enabling spike-to-continuous signal conversion. These neurons serve as the output layer of each module, connecting to the descending pathway, and, in addition to the functional capabilities of the yellow LIF neurons, they also perform information decoding and output.

### B. Cerebellum module

Humans are capable of rapidly acquiring complex skills through imitation, and neural networks exhibit similar properties. Therefore, compared with unsupervised learning approaches, training a neural network to perform gravity compensation via imitation provides a faster and more efficient solution. Under the condition of a known robotic arm dynamics model, the gravity compensation torque represents a nonlinear mapping from joint positions to joint torques. In the machine learning domain, the task of fitting a curve to observed data under supervision is referred to as a regression task, for which

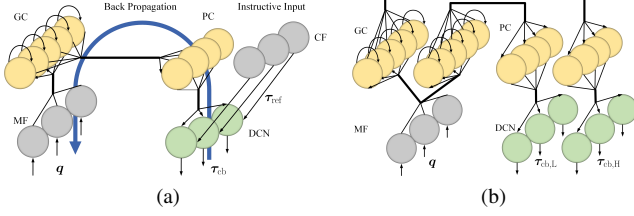


Fig. 2. (a) Structure of one network unit in the cerebellum module during training. (b) Structure of cerebellum network during prediction.

extensive research and mature methods already exist [35], [36].

As shown in Fig.2a, to implement the cerebellum module, a four-layer recurrent SNN is designed as a network unit of the module, analogous to the “microcomplex” proposed in [20], [21]. The input variable  $q \in \mathbb{R}^7$  corresponds to the actual joint positions of the robotic arm, and the output  $\tau_{cb} \in \mathbb{R}^7$  represents the gravity compensation torques under a given load condition.

Variables from the ascending pathway first arrive at the mossy fiber (MF) layer, which is fully connected to the granule cell (GC) layer consisting of 300 LIF neurons. The GC layer, in turn, is fully connected to the Purkinje cell (PC) layer containing 200 LIF neurons. Each PC neuron receives input from both the current and previous time step of the GC layer, capturing temporal dynamics. The output of the PC layer is fully connected to the deep cerebellar nuclei (DCN) layer, which consists of 140 non-spiking LIF neurons. The decoding of the DCN layer is inspired by population coding observed in the motor cortex of animals [37]. Studies have shown that during arm movement in primates, the activity of any single motor cortex neuron does not directly indicate the actual movement direction; however, a weighted sum of vectors corresponding to the preferred directions of a population of neurons yields a vector aligned with the movement direction. Analogously, the 140 DCN neurons are grouped in sets of 20, and their membrane potentials are averaged to obtain a 7-dimensional torque output  $\tau_{cb}$ , i.e.,

$$\tau_{cb,i} = \sum_{j=20 \cdot (i-1)}^{20 \cdot i} u_{DCN,j} \quad (11)$$

where  $\tau_{cb,i}$ ,  $i = 1, \dots, 7$  represents the torque for each joint and  $u_{DCN,j}$ ,  $j = 1, \dots, 140$  denotes the membrane potential of each DCN neuron. The network employs rate-based encoding [38], with a time window of length  $T$ .

The training data  $\tau_{ref}$  are generated using the robotic arm’s dynamics model. Under the condition that the training data adequately cover the workspace, this regression-based approach is sufficient to achieve effective gravity compensation. The network is trained in a supervised manner, with the objective of minimizing the error between the torques output by the network and the reference torques computed from the dynamics model. Structurally, this is reflected in the DCN layer neurons receiving both excitatory inputs from the PC layer neurons and inhibitory inputs from the climbing fiber (CF) neurons. Mathematically, the network output torque  $\tau_{cb}$

is compared with the reference torque  $\tau_{ref}$  to obtain an error, which is quantified using the mean squared error (MSE Loss), i.e.,

$$MSE = \frac{\sum_{i=1}^7 (\tau_{cb,i} - \tau_{ref,i})^2}{7} \quad (12)$$

The weights are then updated via backpropagation, thereby completing the training process; detailed procedures are provided in Algorithm 2.

---

#### Algorithm 2 Training process of one network unit in the cerebellum module

---

- 1: initialize load  $M$ , trajectory length  $L$ , batch size  $bs$ , learning rate  $lr$ , momentum  $mo$ , epochs  $ep$ , random noise  $n$ , network loss  $loss$
  - 2: initialize reference torque  $\tau_{ref}[1 : L]$ , network output torque  $\tau_{cb}[1 : bs]$
  - 3: initialize optimizer  $optim(lr, mo)$
  - 4: initialize network
  - 5: load training trajectory  $q_d[1 : L]$
  - 6: load robotic arm urdf file and initialize dynamic model according to  $M$
  - 7: **for**  $t = 1$  to  $L$  **do**
  - 8:   read joint position  $q_d[t]$
  - 9:   generate reference torque  $\tau_{ref}(q_d[t])$  using dynamic model
  - 10:   update  $\tau_{ref}[t]$
  - 11: **end for**
  - 12: **for**  $i = 1$  to  $ep$  **do**
  - 13:   **for**  $j = 1$  to  $L$  by  $bs$  **do**
  - 14:     update random noise  $n$
  - 15:     add noise to a batch of reference torque  $\tau_{ref,n}[j : j + bs] = \tau_{ref}[j : j + bs] + n$
  - 16:     generate network output  $\tau_{cb}[j : j + bs]$
  - 17:     calculate error between network output and reference torque  $loss(\tau_{ref,n}[j : j + bs], \tau_{cb}[j : j + bs])$
  - 18:     back propagate  $loss$
  - 19:     update network weights using  $optim$
  - 20:   **end for**
  - 21: **end for**
- 

During backpropagation, a surrogate gradient function is employed, given by

$$\sigma(x) = \frac{1}{1 + \exp^{-\nu x}} \quad (13)$$

where  $\nu$  is a scaling factor. In this study, horizontal circular and inclined circular trajectories are used for training, with their mathematical expressions defined as

$$\text{horizontal circle: } \begin{cases} x = x_0 + R_c \cos(\frac{2\pi t}{T_c}) \\ y = y_0 + R_c \sin(\frac{2\pi t}{T_c}) \\ z = z_0 \end{cases} \quad (14)$$

$$\text{inclined circle: } \begin{cases} x = x_1 + R_c \cos(\frac{2\pi t}{T_c}) \cos \theta_0 \\ y = y_1 + R_c \sin(\frac{2\pi t}{T_c}) \\ z = z_1 + R_c \cos(\frac{2\pi t}{T_c}) \sin \theta_0 \end{cases} \quad (15)$$

The parameters of neurons in each layer, as well as other settings used during training, are summarized in Table I.

After training, the network can operate without reference torques, with CF neurons no longer required, relying solely on the learned synaptic weights to generate gravity compensation torques. To accommodate different loads, two network units are trained separately under light (no load) and heavy (3 kg

TABLE I  
TRAINING AND NEURON PARAMETERS OF THE CEREBELLUM MODULE

Training parameter	Value	Neuron parameter	Value
Epochs	50	$u_{\text{reset}}$	GC: 0.0
Learning rate	each trajectory 0.01		PC: 0.0
Momentum	0.5		DCN: 0.0
Noise	$N(0, 1)$	$u_{\text{fire}}$	GC: 0.1
Batch size	10		PC: 0.1
Optimizer	SGD	$\tau_m$	DCN: $\infty$
$\theta_0$	$-\frac{\pi}{6}$		GC: 10.0
$R_c$	0.14		PC: 10.0
$T_c$	3		DCN: 5.0
$(x_0, y_0, z_0)$	(0.54, 0.0, 0.45)		$\nu$
$(x_1, y_1, z_1)$	(0.63, -0.11, 0.3)	$T$	10

load) modes using the supervised learning procedure described in Algorithm 2. These trained networks are then combined to form the complete cerebellum module structure illustrated in Fig. 2b.

In summary, after training, the cerebellum module receives as input the actual joint positions of the robotic arm,  $\mathbf{q} \in \mathbb{R}^7$ , and outputs a gravity compensation matrix composed of two torque vectors, i.e.,  $\mathbf{T}_{\text{cb}} = (\boldsymbol{\tau}_{\text{cb,L}}, \boldsymbol{\tau}_{\text{cb,H}})$ ,  $\boldsymbol{\tau}_{\text{cb,L}} \in \mathbb{R}^7$  and  $\boldsymbol{\tau}_{\text{cb,H}} \in \mathbb{R}^7$ . This matrix corresponds to the learned patterns of the cerebellum module and provides gravity compensation for trajectory tracking tasks under both light and heavy conditions. The outputs are subsequently integrated by the thalamus module to achieve gravity compensation for arbitrary loads within a specified range. During trajectory tracking, the prediction process of the cerebellum module is described in Algorithm 3, which can be implemented as Sub-thread 4 in Algorithm 1.

### Algorithm 3 Prediction process of the cerebellum module

- 1: load the network for light and heavy load conditions
- 2: initialize gravity compensation matrix  $\mathbf{T}_{\text{cb}}$
- 3: read joint position  $\mathbf{q}$
- 4: feed  $\mathbf{q}$  into the two trained network unit, and generate two output  $\boldsymbol{\tau}_{\text{cb,L}}, \boldsymbol{\tau}_{\text{cb,H}}$
- 5: update  $\mathbf{T}_{\text{cb}} = (\boldsymbol{\tau}_{\text{cb,L}}, \boldsymbol{\tau}_{\text{cb,H}})$

### C. Thalamus module

As described in the previous sub-section, although we trained two neural network units under different end-effector load conditions to form the cerebellum module—thereby generating gravity compensation torques corresponding to two specific load cases—the cerebellum module alone remains insufficient for handling arbitrary load. To address this limitation, we developed the thalamus module. By utilizing torque sensor data at the robotic arm’s end-effector, the thalamus module network is able to “sense” the weight of the object, akin to human perception, and accordingly assign adaptive weights to the two gravity compensation torques produced by the cerebellum module’s motor patterns via reinforcement learning. This mechanism enables effective compensation for loads of varying mass and shape.

The thalamus module contains five layers of neurons, as illustrated in Fig. 3. Its input  $\mathbf{F}_{\text{ef}} \in \mathbb{R}^6$  and  $\mathbf{T}_{\text{cb}} = (\boldsymbol{\tau}_{\text{cb,L}}, \boldsymbol{\tau}_{\text{cb,H}}) \in$

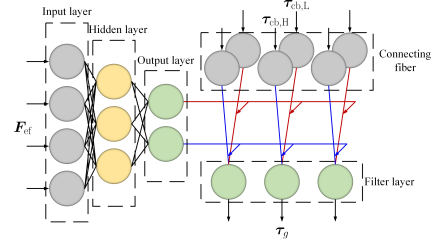


Fig. 3. Structure of thalamus module.

TABLE II  
TRAINING AND NEURON PARAMETERS OF THE THALAMUS MODULE

Parameter	Value	Parameter	Value
Learning rate	0.01	$\nu$	5.0
Weight decay	0.001	$T$	10
Optimizer	SGD	$u_{\text{reset}}$	Hidden layer: 0.0
Momentum	0.5		Output layer: 10.0
$\tau_m$	Hidden layer: 5.0	$u_{\text{fire}}$	Filter layer: 0.0
	Output layer: 5.0		Hidden layer: 0.01
	Filter layer: 5.0		Output layer: $\infty$
			Filter layer: $\infty$

$\mathbb{R}^{7 \times 2}$ , corresponds to the six-dimensional force/torque sensor data measured at the end-effector, and the cerebellum module output, respectively. Its output,  $\mathbf{w} = (w_1, w_2)^T \in \mathbb{R}^2$ , represents the weight coefficients assigned to the two gravity compensation torques provided by the cerebellum module.

The input layer is fully connected to a hidden layer consisting of five LIF neurons, which in turn connects to an output layer of two non-spiking LIF neurons. The membrane potentials of the output neurons are then passed through a Softmax function to produce the two weight coefficients. The loss function designed for this network comprises two terms, minimizing both the joint position error and the joint velocity error, i.e.,

$$\text{Loss} = \sum_{i=1}^7 100 * (q_{d,i} - q_i) + \sum_{i=1}^7 10^{-4} * (\dot{q}_{d,i} - \dot{q}_i) \quad (16)$$

Similar to the cerebellum module, the thalamus module adopts rate-based encoding with a time window length of  $T$ , and employs the sigmoid function as the surrogate gradient function.

After obtaining  $\mathbf{w}$  from the output layer, it is then combined with data from the connecting fiber (linking the thalamus module and the cerebellum module) to generate a weighted output via matrix multiplication, yielding

$$\begin{aligned} \delta \mathbf{u}_{\text{ft}}(t) &= (\delta u_{\text{ft},1}(t), \delta u_{\text{ft},2}(t), \dots, \delta u_{\text{ft},7}(t))^T \\ &= (\boldsymbol{\tau}_{\text{cb,L}}, \boldsymbol{\tau}_{\text{cb,H}}) \cdot \mathbf{w} = w_1 \boldsymbol{\tau}_{\text{cb,L}} + w_2 \boldsymbol{\tau}_{\text{cb,H}} \end{aligned} \quad (17)$$

This weighted result is not directly used as the output; instead, it is injected as an increment to the membrane potentials of seven non-spiking LIF neurons that serve as a filter layer. Specifically, the membrane potential of each filtering-layer

neuron at time  $t$  is given by

$$u_{\text{fit},i}(t) = u_{\text{fit},i}(t-1) - \frac{u_{\text{fit},i}(t-1) - u_{\text{reset}}}{\tau_m} + \frac{\delta u_{\text{fit},i}(t)}{\tau_m}, i = 1, \dots, 7 \quad (18)$$

Finally we take the membrane potential of each filter-layer neuron at time  $t$  as the gravity compensation torque, i.e.,  $\tau_g = \mathbf{u}_{\text{fit}}(t) = (u_{\text{fit},1}(t), u_{\text{fit},2}(t), \dots, u_{\text{fit},7}(t))$ , which is then transmitted to the spinal cord module for further processing. The parameters of the neurons in each layer of this network, as well as the training parameters, are summarized in Table II. During trajectory tracking tasks, the learning procedure of the thalamus module follows Algorithm 4, which can be directly implemented as Sub-thread 3 in Algorithm 1.

---

**Algorithm 4** Training process of the thalamus module

---

- 1: initialize gravity compensation torque  $\tau_g$ , weight coefficients  $\mathbf{w}$ , network loss  $loss$ , optimizer  $optim(lr, mo)$
  - 2: read  $\mathbf{T}_{\text{cb}}, \mathbf{F}_{\text{ef}}$
  - 3: feed  $\mathbf{F}_{\text{ef}}$  into the network and generate weight coefficients  $\mathbf{w}$
  - 4: calculate  $\mathbf{T}_{\text{cb}} \cdot \mathbf{w}$  and feed the result into the filter layer neurons
  - 5: read the membrane potential of the filter layer  $\mathbf{u}_{\text{fit}}$ , update  $\tau_g$
  - 6: read joint position and velocity data  $\hat{\mathbf{q}}_d, \mathbf{q}_d, \dot{\mathbf{q}}, \mathbf{q}$
  - 7: calculate and update  $loss$
  - 8: back propagate  $loss$
  - 9: update network weights using  $optim$
- 

#### D. Brainstem module

As illustrated in Fig. 1c, the primary role of the brainstem module is to dynamically select appropriate feedback control coefficients during operation through learning, thereby compensating for the nonlinear dynamics of the robotic arm and the coupling effects among joints. The network is implemented as a three-layer fully connected SNN. Its input variable  $[\mathbf{q}_d, \dot{\mathbf{q}}_d, \mathbf{q}, \dot{\mathbf{q}}] \in \mathbb{R}^{28}$  is a concatenated vector consisting of the desired joint positions and velocities, as well as the actual joint positions and velocities. The output  $\mathbf{K} = (k_{p,1}, k_{p,2}, \dots, k_{p,7}, k_{v,1}, k_{v,2}, \dots, k_{v,7}) \in \mathbb{R}^{14}$  corresponds to the proportional and derivative coefficients for each of the seven joints.

The input vector is fully connected to a hidden layer of 10 LIF neurons, which in turn is fully connected to an output layer of 14 non-spiking LIF neurons. The network is trained using reinforcement learning, with the loss function defined as

$$\text{Loss} = \sum_{i=1}^7 100 * (q_{d,i} - q_i) + \sum_{i=1}^7 10^{-4} \cdot (\dot{q}_{d,i} - \dot{q}_i) + \sum_{i=1}^7 10^{-3} \cdot \tau_i^2 \quad (19)$$

In this formulation, the first term minimizes the position error and the second term minimizes the velocity error, ensuring accurate trajectory tracking, while the third term penalizes torque usage to reduce joint energy consumption and prevent abrupt fluctuations in joint torque. Through this design, the network is able to learn feedback control coefficients that

TABLE III  
TRAINING AND NEURON PARAMETERS OF THE BRAINSTEM MODULE

Parameter	Value	Parameter	Value
Learning Rate	0.01	$u_{\text{reset}}$	Hidden layer: 0.0
Momentum	0.5		Output layer: 10.0
Optimizer	SGD	$u_{\text{fire}}$	Hidden layer: 0.005
$\nu$	5.0		Output layer: $\infty$
(a,b)	(20,2)	$\tau_m$	Hidden layer: 5.0
$T$	15		Output layer: 5.0

balance trajectory-tracking accuracy with reduced joint wear and energy cost.

Similar to the cerebellum module, the brainstem module adopts rate-based encoding with a time window length of  $T$ , and the approximate gradient function is chosen as the sigmoid function.

After decoding through the non-spiking LIF neurons in the output layer, we obtain a set of membrane potentials  $\mathbf{u}_{\text{bs}} = (u_{\text{bs},1}, \dots, u_{\text{bs},14}) \in \mathbb{R}^{14}$ . By applying a scaling transformation, these membrane potentials can be mapped to the proportional and derivative coefficients, i.e.,

$$\mathbf{K}_P = \text{diag}(k_{p,1}, k_{p,2}, \dots, k_{p,7}) = a \cdot \text{diag}(u_{\text{bs},1}, u_{\text{bs},2}, \dots, u_{\text{bs},7}) \quad (20)$$

$$\mathbf{K}_V = \text{diag}(k_{v,1}, k_{v,2}, \dots, k_{v,7}) = b \cdot \text{diag}(u_{\text{bs},8}, u_{\text{bs},9}, \dots, u_{\text{bs},14}) \quad (21)$$

where  $a$  and  $b$  are two scaling parameters. The parameters of the neurons in each layer of the network, as well as the parameters used during training, are summarized in Table III.

During trajectory tracking tasks, the learning process of the brainstem module is described in Algorithm 5, which can be implemented as Sub-thread 2 within Algorithm 1.

---

**Algorithm 5** Training process of the brainstem module

---

- 1: initialize coefficients  $\mathbf{K}_V, \mathbf{K}_P$ , network loss  $loss$ , optimizer  $optim(lr, mo)$
  - 2: read joint position and velocity data  $\hat{\mathbf{q}}_d, \mathbf{q}_d, \dot{\mathbf{q}}, \mathbf{q}$
  - 3: feed  $[\mathbf{q}_d, \dot{\mathbf{q}}_d, \mathbf{q}, \dot{\mathbf{q}}]$  into the network
  - 4: read the potential of the output layer neurons  $\mathbf{u}_{\text{bs}}$  and scale them through scaling parameters
  - 5: update  $\mathbf{K}_V, \mathbf{K}_P$
  - 6: read joint position and velocity data  $\hat{\mathbf{q}}_d, \mathbf{q}_d, \dot{\mathbf{q}}, \mathbf{q}$
  - 7: calculate and update  $loss$
  - 8: back propagate  $loss$
  - 9: update network weights using  $optim$
- 

#### E. Spinal cord module

The primary function of the spinal cord module is to integrate proprioceptive information with the outputs of the aforementioned higher-level motor control modules, thereby generating real-time motion control commands. Its structural design is illustrated in Fig. 1c. For high-performance robotic manipulators, torque control typically requires the control algorithm to achieve frequencies of 1000 Hz, 1200 Hz, or even higher. Consequently, the spinal cord module must exhibit very high computational efficiency.

In our design, the input variables  $[q_d, \dot{q}_d, q, \dot{q}] \in \mathbb{R}^{28}$  consist of the planned positions and velocities as well as the actual positions and velocities of all joints, while the output  $\tau \in \mathbb{R}^7$  represents the control torque for each joint. After entering the spinal cord module, the planned trajectory and proprioceptive feedback are first encoded into discrete spike trains, with each joint being processed independently. Specifically, the planned position and velocity signals  $q_{d,i}, \dot{q}_{d,i}, i = 1, \dots, 7$  serve to excite the input fibers, whereas the actual proprioceptive feedback  $q_i, \dot{q}_i, i = 1, \dots, 7$  inhibits the input fibers. Mathematically, this process is equivalent to computing their difference.

The outputs of the input fibers are subsequently passed into the Poisson encoding stage, given by

$$s_{q,i,j} = \begin{cases} 0, & -u_j < \frac{q_{d,i} - q_i}{\Delta q_i} < u_j, j = 1, \dots, n \\ 1, & \frac{q_{d,i} - q_i}{\Delta q_i} \geq u_j, j = 1, \dots, \frac{n}{2} \\ -1, & -\frac{q_{d,i} - q_i}{\Delta q_i} \geq u_j, j = \frac{n}{2}, \dots, n \end{cases} \quad (22)$$

$$s_{\dot{q},i,j} = \begin{cases} 0, & -u_j < \frac{\dot{q}_{d,i} - \dot{q}_i}{\Delta \dot{q}_i} < u_j, j = 1, \dots, n \\ 1, & \frac{\dot{q}_{d,i} - \dot{q}_i}{\Delta \dot{q}_i} \geq u_j, j = 1, \dots, \frac{n}{2} \\ -1, & -\frac{\dot{q}_{d,i} - \dot{q}_i}{\Delta \dot{q}_i} \geq u_j, j = \frac{n}{2}, \dots, n \end{cases} \quad (23)$$

Here,  $u_j \sim U(0, 1), j = 1, \dots, n$  denotes  $n$  independent uniformly distributed random variables,  $s_{q,i,j}, i = 1, \dots, 7, j = 1, \dots, n$  represents the spike trains encoding the position information of each joint at the current time step, and  $s_{\dot{q},i,j}, i = 1, \dots, 7, j = 1, \dots, n$  denotes the spike trains encoding the velocity information. The terms  $\Delta q_i$  and  $\Delta \dot{q}_i, i = 1, \dots, 7$  correspond to the maximum allowable position and velocity errors for each joint, respectively.

From an intuitive perspective, each input fiber is connected to a group of  $n$  submodules, where the first half  $\frac{n}{2}$  are responsible for processing positive inputs and the second half  $\frac{n}{2}$  handle negative inputs. This structure corresponds to the agonist–antagonist pairing characteristic of human muscles. Each submodule generates a uniformly distributed random number in the range  $[0, 1]$ . When the output of the input fiber is positive, the first  $\frac{n}{2}$  neurons are encoded sequentially: if the absolute value of the input exceeds the random number, the encoding result is set to 1; otherwise, it is 0. Conversely, when the output of the input fiber is negative, the second  $\frac{n}{2}$  neurons are encoded sequentially: if the absolute value of the input exceeds the random number, the encoding result is set to  $-1$ ; otherwise, it is 0. This encoding scheme can be implemented in hardware using simple logic gate circuits, thereby achieving very high computational efficiency.

The encoding precision is influenced by three parameters:  $\Delta q_i, \Delta \dot{q}_i, i = 1, \dots, 7$ , and  $n$ . Smaller values of  $\Delta q_i$  and  $\Delta \dot{q}_i$  lead to higher encoding precision, but reduce the range of representable errors; a larger  $n$  increases encoding precision but reduces computational efficiency.

Following this encoding process, two sets of discrete spike trains are generated—one representing position information and the other representing velocity information. These spike trains are then transmitted to stimulate the activity of non-spiking LIF neurons in the output layer, with stimulation strength modulated by the feedback control gains  $k_{p,i}$  and  $k_{v,i}$ ,

TABLE IV  
NEURON PARAMETERS OF THE SPINAL CORD MODULE

Parameter	Value	Parameter	Value
$u_{\text{reset}}$	0.0	$\Delta q_i, i = 1, \dots, 7$	0.5
$u_{\text{fire}}$	$\infty$	$\Delta \dot{q}_i, i = 1, \dots, 7$	0.5
$\tau_m$	2.0	$n$	100

$i = 1, \dots, 7$  provided by the brainstem module, as illustrated by the blue and red dashed lines, respectively. Accordingly, at each time step, the membrane potential increments of the output non-spiking LIF neurons can be expressed as

$$\delta u_{\text{sp},i}(t) = \tau_{g,i} + k_{p,i} \cdot \sum_{j=1}^{100} s_{q,i,j} + k_{v,i} \cdot \sum_{j=1}^{100} s_{\dot{q},i,j}, i = 1, \dots, 7 \quad (24)$$

Here,  $\tau_g = (\tau_{g,1}, \tau_{g,2}, \dots, \tau_{g,7})$  denotes the gravity compensation torque generated by the thalamus module. Consequently, the membrane potentials at each time step can be written as

$$u_{\text{sp},i}(t) = u_{\text{sp},i}(t-1) - \frac{u_{\text{sp},i}(t-1) - u_{\text{reset}}}{\tau_m} + \frac{\delta u_{\text{sp},i}(t)}{\tau_m}, i = 1, \dots, 7 \quad (25)$$

Finally, similar to the thalamus module, we take  $\tau = \mathbf{u}_{\text{sp}} = (u_{\text{sp},1}(t), u_{\text{sp},2}(t), \dots, u_{\text{sp},7}(t))$  as the final control torque, which will be sent in real time to the actuators. The neuronal parameters of the spinal cord module are summarized in Table IV.

Through this mechanism, the output torque at each time step incorporates both the current information and the historical information over a preceding time window, thereby making it more suitable than ANN for time-continuous tasks such as robotic control. During trajectory tracking tasks, the operational process of the spinal cord module is illustrated in Algorithm 6, which can be implemented as Sub-thread 1 within Algorithm 1.

---

#### Algorithm 6 Prediction process of the spinal cord module

---

- 1: initialize control torque  $\tau$
  - 2: read joint position and velocity data  $\dot{q}_d, q_d, \dot{q}, q$
  - 3: read proportional and derivative coefficients  $K_V, K_P$  and gravity compensation torque  $\tau_g$
  - 4: poisson encode  $\dot{q}_d, q_d, \dot{q}, q$  to generate two sets of spike trains  $[s_{q,i,j}], [s_{\dot{q},i,j}]$
  - 5: modulate the spike trains with  $K_V, K_P$
  - 6: feed  $\tau_g$  and the modulated spike trains into the non-spiking LIF neurons
  - 7: read potential and update  $\tau$
- 

## IV. SIMULATION ANALYSIS

To evaluate the rationality and effectiveness of the proposed framework, we conduct three simulation experiments that demonstrate contributions (1)–(3). In section IV-A and IV-B,

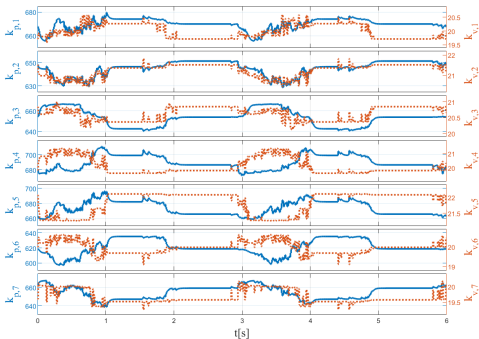


Fig. 4. Average feedback control coefficients of each joint across 3 trajectory tracking tasks.

we validate the design of the modules and in section IV-C, the design of the framework.

The algorithm is implemented in Python (version 3.12.4), and all neural networks are constructed using PyTorch [39] (version 2.4.0). The spiking neurons involved in the algorithm are implemented with the SNN learning framework Spiking-Jelly [40] (version 0.0.0.14). The simulation environment employed is PyBullet [41] (version 3.2.6), an open-source robotics simulation tool whose underlying physics engine is based on the open-source Bullet Physics SDK. The controlled robotic arm consists of seven actuated joints, seven links and a six-dimensional torque sensor mounted at the flange of the end-effector. The control cycle of each layer is set as  $T_1 = 1\text{ms}$ ,  $T_2 = 10\text{ms}$ ,  $T_3 = 50\text{ms}$ . The simulation time step is set to 1 ms, and the control frequency is configured to 1 kHz.

In all simulation experiments presented in this section, trajectory tracking accuracy is evaluated using the root-mean-square error (RMSE) of the joint positions. The RMSE at each time step is defined as

$$\text{RMSE}(t) = \sqrt{\sum_{i=1}^7 (q_{d,i}(t) - q_i(t))^2} \quad (26)$$

while the average RMSE over an entire trajectory is defined as

$$\text{RMSE} = \frac{1}{N} \sum_{t=1}^N \text{RMSE}(t) \quad (27)$$

Three types of trajectories are employed in the simulations: horizontal circle, inclined circle, and spatial figure-eight. The first two trajectories have already been defined in section III-B, while the third trajectory is defined as

$$\text{spatial figure-eight: } \begin{cases} x = x + 0.5R \sin(\frac{4\pi t}{T}) \\ y = y + R \cos(\frac{2\pi t}{T}) \\ z = z + z \sin(\frac{2\pi t}{T}) \end{cases} \quad (28)$$

where  $x = 0.61$ ,  $y = 0$ ,  $z = 0.3$ ,  $R = 0.14$ ,  $T = 3$ ,  $z = 0.08$ .

#### A. Spinal cord and brainstem module validation

Physiological studies have demonstrated that joint stiffness and damping in the human arm exhibit an inverse correlation

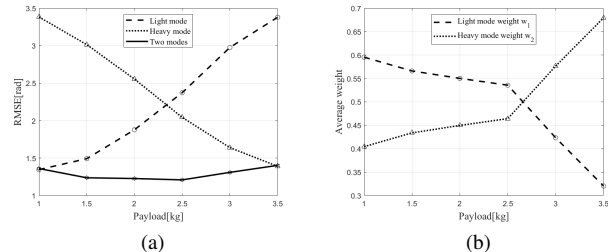


Fig. 5. (a) Average tracking error using single mode and two modes across three trajectories. (b) Average weight generated by the thalamus module across three trajectories.

[42]. Specifically, stiffness decreases when a joint begins to move and increases when at rest, while damping decreases as the joint approaches a target and increases at the onset of motion. In the proposed framework, the feedback control coefficients  $K_V$  and  $K_P$  generated by the brainstem module correspond precisely to damping and stiffness in feedback control. Fig. 4 illustrates the variations of average  $k_p$  (blue solid lines) and  $k_v$  (red dashed lines) for each joint across three trajectories. It can be observed that the two parameters generally exhibit opposite trends, as exemplified by joints 3–6 during 3–5 s and joints 4 and 6 during 1–2 s. This finding indicates that the brainstem module, through reinforcement learning, adjusts joint stiffness and damping in the spinal module in a manner that exhibits biomimetic characteristics, consistent with our design objectives. We also note that this feature is less pronounced in joints closer to the robot’s base, such as joints 1 and 2, likely due to stronger coupling effects from adjacent joints.

#### B. Thalamus and cerebellum module validation

Fig. 5a shows that single gravity compensation modes from the cerebellum module are only effective within narrow load ranges (e.g., the light mode around 1 kg and the heavy mode around 3.5 kg), with errors otherwise increasing nearly linearly with load variation. In contrast, the thalamus module adaptively synthesizes both modes, maintaining stable joint error across the entire 1–3.5 kg range, thereby validating its design. As shown in Fig. 5b, reinforcement learning enables the thalamus module to adjust mode weights according to load mass, assigning a smaller weight to the light mode and a greater weight to the heavy mode as the load increases. This adaptive mechanism mirrors human motor control, where movements are achieved through linear combinations of motor primitives [43], thus highlighting the biomimetic nature of the thalamus and cerebellum module.

#### C. Framework validation

Fig. 6 illustrates the average trajectory tracking error across three trajectories under different load conditions. As shown in Fig. 6a, when a 1.5kg load is applied at 0s, the algorithm converges to a stable state within approximately 1.5s; after 12s of operation, adding an additional 2kg load again leads to convergence within about 2s; and upon removing

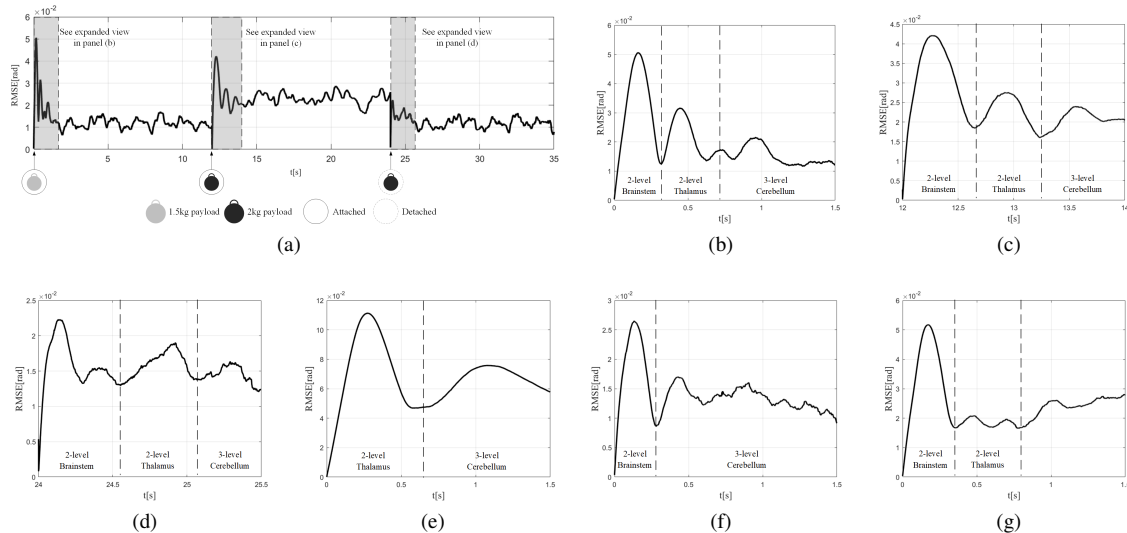


Fig. 6. Average joint error across the three trajectories under varying load conditions during operation. (a) 0-1.5s. (b) 12-14s. (c) 24-25.5s. (d) 0-1.5s without the brainstem module. (e) 0-1.5s without the thalamus module. (f) 0-1.5s without the cerebellum module.

the added load at 24s, convergence is also achieved within 2s. In contrast, the cerebellum-inspired network proposed in [20], [21] requires nearly 100s to adapt to a 500g change in load, highlighting the superior dynamic performance and convergence speed of our framework. Furthermore, we observe that, compared with cold-start initialization, subsequent load changes during ongoing operation induce smaller error fluctuations, as reflected by reduced peak magnitude at 12s and 24s, which can be attributed to the membrane potential dynamics of spiking neurons that preserve historical information and facilitate smoother adaptation.

Fig. 6b, 6c and 6d further show that the convergence process consistently exhibits three distinct error peaks following each load change. These peaks directly correspond to the hierarchical loop structure of the framework: the spinal cord module (first-order level) updates at the control frequency and therefore corresponds to every point on the curve; the brainstem and thalamus modules (second-order level) yield the earlier two peaks which reflect the learning convergence process; and the cerebellum module (third-order level) produces the latest peak owing to its longest processing cycle. The temporal separation of these peaks validates the layered organization of the control framework.

To verify this correspondence, ablation experiments were conducted by selectively disabling individual modules, as shown in Fig. 6e, 6f and 6g. Removing the brainstem’s learning capability by fixing feedback control coefficients reduces the number of peaks to two and delays the first peak, indicating diminished adaptability to load change. Similarly, disabling the thalamus module by fixing mode-combination weights eliminates its characteristic peak, leaving only brainstem and cerebellar responses. Finally, replacing the cerebellum’s adaptive torque generation with fixed compensation suppresses the cerebellar peak and weakens the thalamic one, since the thalamus relies on cerebellar outputs to optimize weight assignment. These results confirm the functional contributions of each module and their hierarchical cooperation.



Fig. 7. The experiment setting.

In summary, the proposed framework exhibits robust adaptability and rapid convergence to load variations, with distinct loop-specific responses emerging in a biologically consistent sequence. This step-by-step activation phenomenon mirrors the progression of human neural responses to perturbations, namely M1 reflexes, M2 reflexes, and voluntary movements [44], thereby reinforcing the plausibility and effectiveness of the neuromorphic design.

## V. EXPERIMENT RESULTS

This section will present real-world experiments on a robotic arm platform to demonstrate contribution (4). All spiking neurons, except those in the spinal cord module, are implemented in Python using an open-source SNN learning framework, while the spinal cord module is realized in C++ through direct modeling of membrane potential dynamics. The deep learning framework, SNN framework, and computing hardware are identical to that used in the simulation. The robotic arm platform is a Flexiv Rizon 4s equipped with a Flexiv GRAV gripper, as shown in Fig. 7.

The experiments are conducted under nine load conditions, including two material types (sand-filled and water-filled containers) and five mass levels ranging from 1.5 kg (gripper with empty container) to 3.5 kg (container with 2 kg load). The

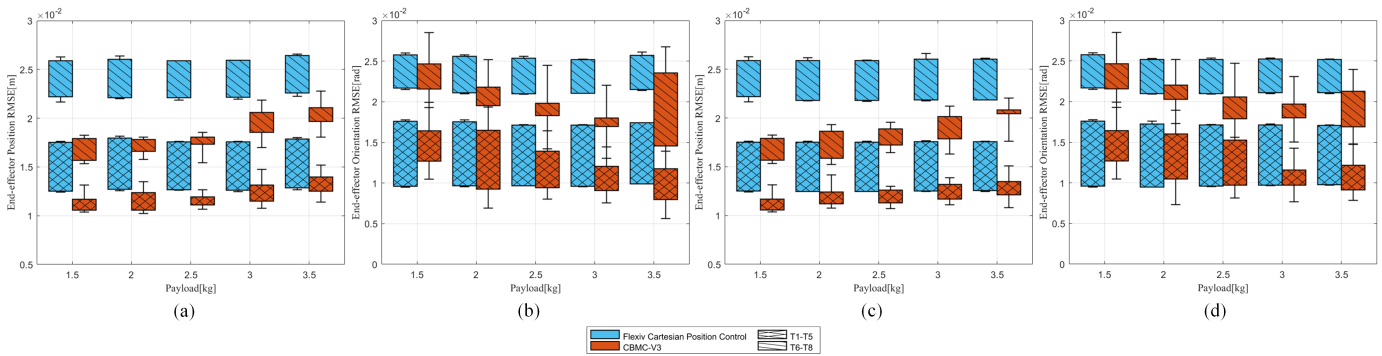


Fig. 8. Trajectory tracking result under different trajectory and load conditions. (a) Position RMSE under sand load. (b) Orientation RMSE under sand load. (c) Position RMSE under water load. (d) Orientation RMSE under water load.

upper limit is chosen below the 4 kg load capacity of the robotic platform to maintain a safety margin.

Eight end-effector trajectories (T1–T8, defined in the Appendix) are tested, all with vertically downward orientation and origin at the base flange center. Among them, T1–T5 represent slower, lower-dynamic trajectories, while T6–T8 correspond to faster, higher-dynamic ones. For statistical validity, each trajectory–load–controller combination is repeated 10 times. In all experiments presented in this section, the trajectory tracking effect is evaluated using the RMSE of the end-effector position and orientation. At each time step, the position and orientation RMSE are defined as

$$\text{RMSE}_p(t) = \sqrt{(x_d(t) - x(t))^2 + (y_d(t) - y(t))^2 + (z_d(t) - z(t))^2} \quad (29)$$

$$\text{RMSE}_o(t) = \sqrt{(\theta_d(t) - \theta(t))^2 + (\psi_d(t) - \psi(t))^2 + (\phi_d(t) - \phi(t))^2} \quad (30)$$

where  $x_d, y_d, z_d, \theta_d, \psi_d, \phi_d$  denote the desired end-effector position in Cartesian space and the desired pitch, yaw, and roll angles, respectively, and  $x, y, z, \theta, \psi, \phi$  denote the corresponding actual values. The average position and orientation RMSE of a trajectory are defined as

$$\text{RMSE}_p = \frac{1}{N} \sum_{t=1}^N \text{RMSE}_p(t) \quad (31)$$

$$\text{RMSE}_o = \frac{1}{N} \sum_{t=1}^N \text{RMSE}_o(t) \quad (32)$$

where  $N$  represents the trajectory length.

Fig. 8a and 8b show the trajectory tracking errors of the robotic arm when the end-effector container is filled with sand, under various trajectory and load conditions. Red and blue bars represent the proposed method and the factory-installed industrial-grade Flexiv Cartesian Position Control, respectively. Cross-hatched and slanted-hatched bars indicate the error ranges of trajectories T1–T5 (lower dynamic group) and T6–T8 (higher dynamic group) for a given load, while error bars denote the extrema of the errors. Four observations can be drawn:

1. Higher tracking accuracy: For any load mass, the proposed method yields smaller mean position and orientation errors, as indicated by the consistently lower red bars compared

with the blue bars. Quantitatively, the Flexiv method achieves average errors of  $1.789 \times 10^{-2}$  m (position) and  $1.685 \times 10^{-2}$  rad (orientation) across all trajectories and load conditions, whereas the proposed method achieves  $1.447 \times 10^{-2}$  m and  $1.473 \times 10^{-2}$  rad, corresponding to reductions of 19.1% and 12.6%, respectively. These results demonstrate that the proposed method achieves higher control accuracy, thereby exhibiting superiority in the “Precision” indicator of agility.

2. Adaptation to load variation: As load mass increases, position errors of the proposed method gradually increase while orientation errors decrease, and both remain generally lower than those of the Flexiv method, as shown by the upward trend of red bars in Fig. 8a and the downward trend in Fig. 8b. This observation is consistent with the simulation results, confirming that the proposed framework can adapt to arbitrary load masses within a practical range, validating the design of the cerebellar and thalamic modules.

3. Consistency across trajectories: Within each trajectory group of similar dynamics, the proposed method exhibits greater consistency across different trajectory shapes, as the red bars for both hatching styles are shorter than their blue counterparts. Specifically, the variation ranges of Flexiv errors in position and orientation are  $0.447 \times 10^{-2}$  m and  $0.592 \times 10^{-2}$  rad, while those of the proposed method are  $0.152 \times 10^{-2}$  m and  $0.363 \times 10^{-2}$  rad, corresponding to reductions of 66.0% and 38.7%. This aligns with simulation findings, indicating that the proposed method can rapidly adapt online to arbitrary motion patterns, validating the brainstem and spinal cord modules and demonstrating an advantage in the agility indicator of “Transitions between diverse motion patterns”.

4. Performance under higher dynamics: For the higher-dynamic group, the performance improvement of the proposed method is more pronounced, as the gap between red and blue slanted bars is larger than that between the cross-hatched bars. Quantitatively, in the higher-dynamic group, the proposed method reduces position and orientation errors by 24.7% and 17.0% relative to the Flexiv method, exceeding the average improvements reported in conclusion 1. This outcome is expected, since the Flexiv method, being model-based, necessarily involves linear simplifications to ensure computational efficiency. While such simplifications suffice

at low speeds where nonlinear effects (e.g., Coriolis and centrifugal forces) are weak, they deteriorate at higher speeds. In contrast, the proposed method adapts online to nonlinear dynamics, leading to smaller error increases. These results suggest that the proposed framework is more suitable for fast motions, demonstrating superiority in the agility indicator of “Speed”.

Fig. 8c and 8d present results when the container is filled with water. Compared to sand, water introduces stronger dynamic variations, thereby exerting greater influence on control performance. The proposed method yields mean errors of  $1.442 \times 10^{-2}$  m (position) and  $1.519 \times 10^{-2}$  rad (orientation), representing increases of 0.9% and 2.0% relative to the sand condition; the Flexiv method yields  $1.779 \times 10^{-2}$  m and  $1.681 \times 10^{-2}$  rad, representing decreases of 1.2% and 0.7%, respectively. Both methods show comparable trends across different load materials, indicating the ability to adapt to varying material properties. Moreover, the proposed method consistently demonstrates similar control performance under sand and water conditions, and analogous conclusions to the four points above can be drawn, which are omitted here for brevity.

In summary, the experiment results demonstrate that the proposed framework consistently outperforms the industrial-grade control algorithm across the three key indicators of agility—precision, adaptability to diverse motion patterns, and speed as mentioned in section I—thereby highlighting its effectiveness and the enhanced agility capacity provided by the brain-inspired design.

## VI. CONCLUSION AND FUTURE WORKS

In this paper, we propose a CNS-inspired control framework based on SNN, enabling agile robotic arm control in complex environments. The framework introduces a hierarchical architecture with five modules implemented using SNNs, and has been validated through both simulations and real-world robotic experiments. Results show that this framework operates in a manner similar to the human CNS and can outperform an industrial-grade baseline. Future work will focus on improving reinforcement learning for higher reproducibility, enhancing the cerebellar module for better gravity compensation, and further increasing control accuracy.

## APPENDIX

### EXPERIMENT TRAJECTORY SETTING

$$\text{T1: } \begin{cases} x = x_0 + R_0 \cos(\frac{2\pi t}{T_0}) \\ y = y_0 + R_0 \sin(\frac{2\pi t}{T_0}) \\ z = z_0 \end{cases} \quad \text{T2: } \begin{cases} x = x_1 \\ y = y_1 + R_1 \sin(\frac{2\pi t}{T_1}) \\ z = z_1 + R_1 \cos(\frac{2\pi t}{T_1}) \end{cases}$$

$$\text{T3: } \begin{cases} x = x_2 + R_2 \cos(\frac{2\pi t}{T_2}) \cos \theta_1 \\ y = y_2 + R_2 \sin(\frac{2\pi t}{T_2}) \\ z = z_2 + R_2 \cos(\frac{2\pi t}{T_2}) \sin \theta_1 \end{cases}$$

$$\text{T4: } \begin{cases} x = x_3 + 0.5R_3 \sin(\frac{4\pi t}{T_3}) \\ y = y_3 + R_3 \cos(\frac{2\pi t}{T_3}) \\ z = z_3 + z \sin(\frac{2\pi t}{T_3}) \end{cases}$$

TABLE V  
TRAJECTORY PARAMETERS

Parameter	Value	Parameter	Value	Parameter	Value
$(x_0, y_0, z_0)$	(0.54,0.0, 0.45) m	$R_0$	0.14 m	$T_0$	4 s
$(x_1, y_1, z_1)$	(0.6,0.35, 0.0) m	$R_1$	0.2 m	$T_1$	4 s
$(x_2, y_2, z_2)$	(0.63,-0.11, 0.3) m	$R_2$	0.14 m	$T_2$	4 s
$(x_3, y_3, z_3)$	(0.0,0.61, 0.3) m	$R_3$	0.14 m	$T_3$	4s
$(x_4, y_4, z_4)$	(0.53,-0.11, 0.4) m	$R_4$	0.2 m	$T_4$	3s
$(x_5, y_5, z_5)$	(0.53,-0.11, 0.4) m	$R_5$	0.2 m	$T_5$	2s
$\theta_1$	$-\frac{\pi}{6}$ rad	$\phi_1$	$\frac{\pi}{3}$ rad	$T_6$	3s
$\theta_2$	$\frac{\pi}{6}$ rad			$T_7$	3s

$$\text{T5: } \begin{cases} x = x_3 + 0.5R_3 \sin(\frac{4\pi t}{T_4}) \\ y = y_3 + R_3 \cos(\frac{2\pi t}{T_4}) \\ z = z_3 + z \sin(\frac{2\pi t}{T_4}) \end{cases}$$

$$\text{T6: } \begin{cases} x = x_2 + R_2 \cos(\frac{2\pi t}{T_5}) \cos \theta_1 \\ y = y_2 + R_2 \sin(\frac{2\pi t}{T_5}) \\ z = z_2 + R_2 \cos(\frac{2\pi t}{T_5}) \sin \theta_1 \end{cases}$$

$$\text{T7: } \begin{cases} x = x_4 + R_4 \cos(\frac{2\pi t}{T_6}) \cos \theta_2 \\ y = y_4 + R_4 \sin(\frac{2\pi t}{T_6}) \\ z = z_4 + R_4 \cos(\frac{2\pi t}{T_6}) \sin \theta_2 \end{cases}$$

$$\text{T8: } \begin{cases} x = x_5 + R_5 \cos(\frac{2\pi t}{T_7}) \cos \theta_2 \cos \phi_1 - R_4 \sin(\frac{2\pi t}{T_7}) \sin \phi_1 \\ y = y_5 + R_5 \cos(\frac{2\pi t}{T_7}) \cos \theta_2 \sin \phi_1 + R_4 \sin(\frac{2\pi t}{T_7}) \cos \phi_1 \\ z = z_5 + R_5 \cos(\frac{2\pi t}{T_7}) \sin \theta_2 \end{cases}$$

## REFERENCES

- [1] M. T. Mason, “Toward robotic manipulation,” *Annual Review of Control, Robotics, and Autonomous Systems*, vol. 1, pp. 1–28, 2018.
- [2] Y. Abe, M. da Silva, and J. Popović, “Multiobjective control with frictional contacts,” in *Proceedings of the 2007 ACM SIGGRAPH/Eurographics Symposium on Computer Animation*, ser. SCA ’07. Goslar, DEU: Eurographics Association, 2007, p. 249–258.
- [3] M. Liu, A. Micaelli, P. Evrard, A. Escande, and C. Andriot, “Interactive dynamics and balance of a virtual character during manipulation tasks,” in *2011 IEEE International Conference on Robotics and Automation*. IEEE, 2011, pp. 1676–1682.
- [4] J. Salini, V. Padois, and P. Bidaud, “Synthesis of complex humanoid whole-body behavior: A focus on sequencing and tasks transitions,” in *2011 IEEE International Conference on Robotics and Automation*, 2011, pp. 1283–1290.
- [5] J. Lee, N. Mansard, and J. Park, “Intermediate desired value approach for task transition of robots in kinematic control,” *IEEE Transactions on Robotics*, vol. 28, no. 6, pp. 1260–1277, 2012.
- [6] A. Escande, N. Mansard, and P.-B. Wieber, “Hierarchical quadratic programming: Fast online humanoid-robot motion generation,” *The International Journal of Robotics Research*, vol. 33, no. 7, pp. 1006–1028, 2014.
- [7] S. Kim, K. Jang, S. Park, Y. Lee, S. Y. Lee, and J. Park, “Continuous task transition approach for robot controller based on hierarchical quadratic programming,” *IEEE Robotics and Automation Letters*, vol. 4, no. 2, pp. 1603–1610, 2019.
- [8] G. Han, J. Wang, X. Ju, and M. Zhao, “Recursive hierarchical projection for whole-body control with task priority transition,” *arXiv preprint arXiv:2109.07236*, 2021.

- [9] A. Carron, E. Arcari, M. Wermelinger, L. Hewing, M. Hutter, and M. N. Zeilinger, "Data-driven model predictive control for trajectory tracking with a robotic arm," *IEEE Robotics and Automation Letters*, vol. 4, no. 4, pp. 3758–3765, 2019.
- [10] J. Pankert and M. Hutter, "Perceptive model predictive control for continuous mobile manipulation," *IEEE Robotics and Automation Letters*, vol. 5, no. 4, pp. 6177–6184, 2020.
- [11] Y. Wang, Y. Pang, Q. Li, W. Cai, and M. Zhao, "Trajectory tracking control for robot manipulator under dynamic environment," in *International Conference on Intelligent Robotics and Applications*. Springer, 2023, pp. 513–524.
- [12] H. Chaoui, P. Sicard, and W. Gueaieb, "Ann-based adaptive control of robotic manipulators with friction and joint elasticity," *IEEE Transactions on Industrial Electronics*, vol. 56, no. 8, pp. 3174–3187, 2009.
- [13] W. He and Y. Dong, "Adaptive fuzzy neural network control for a constrained robot using impedance learning," *IEEE transactions on neural networks and learning systems*, vol. 29, no. 4, pp. 1174–1186, 2017.
- [14] F. Wang, Z. Liu, C. P. Chen, and Y. Zhang, "Adaptive neural network-based visual servoing control for manipulator with unknown output nonlinearities," *Information Sciences*, vol. 451, pp. 16–33, 2018.
- [15] T. Sallloom, X. Yu, W. He, and O. Kaynak, "Adaptive neural network control of underwater robotic manipulators tuned by a genetic algorithm," *Journal of Intelligent & Robotic Systems*, vol. 97, pp. 657–672, 2020.
- [16] C. Liu, Z. Zhao, and G. Wen, "Adaptive neural network control with optimal number of hidden nodes for trajectory tracking of robot manipulators," *Neurocomputing*, vol. 350, pp. 136–145, 2019.
- [17] D. T. Pham, T. V. Nguyen, H. X. Le, L. Nguyen, N. H. Thai, T. A. Phan, H. T. Pham, A. H. Duong, and L. T. Bui, "Adaptive neural network based dynamic surface control for uncertain dual arm robots," *International Journal of Dynamics and Control*, vol. 8, pp. 824–834, 2020.
- [18] Z. Bing, C. Meschede, F. Röhrbein, K. Huang, and A. C. Knoll, "A survey of robotics control based on learning-inspired spiking neural networks," *Frontiers in neurorobotics*, vol. 12, p. 35, 2018.
- [19] R. R. Carrillo, E. Ros, C. Boucheny, and J.-M. C. Olivier, "A real-time spiking cerebellum model for learning robot control," *Biosystems*, vol. 94, no. 1–2, pp. 18–27, 2008.
- [20] I. Abadía, F. Naveros, J. A. Garrido, E. Ros, and N. R. Luque, "On robot compliance: A cerebellar control approach," *IEEE transactions on cybernetics*, vol. 51, no. 5, pp. 2476–2489, 2019.
- [21] I. Abadía, F. Naveros, E. Ros, R. R. Carrillo, and N. R. Luque, "A cerebellar-based solution to the nondeterministic time delay problem in robotic control," *Science Robotics*, vol. 6, no. 58, p. eabf2756, 2021.
- [22] I. Abadía, A. Bruel, G. Courtine, A. J. Ijspeert, E. Ros, and N. R. Luque, "A neuromechanics solution for adjustable robot compliance and accuracy," *Science Robotics*, vol. 10, no. 98, p. eadp2356, 2025. [Online]. Available: <https://www.science.org/doi/abs/10.1126/scirobotics.adp2356>
- [23] M. M. Halassa, *The Thalamus*. Cambridge University Press, 2022.
- [24] Q. Li, Y. Pang, Y. Wang, X. Han, Q. Li, and M. Zhao, "Cbmc: A biomimetic approach for control of a 7-degree of freedom robotic arm," *Biomimetics*, vol. 8, no. 5, p. 389, 2023.
- [25] Y. Pang, Q. Li, Y. Wang, and M. Zhao, "Cbmc-v2: A cns-inspired framework for real-time robotic arm control," in *2024 IEEE-RAS 23rd International Conference on Humanoid Robots (Humanoids)*, 2024, pp. 121–128.
- [26] P. Eckert and A. J. Ijspeert, "Benchmarking agility for multilegged terrestrial robots," *IEEE Transactions on Robotics*, vol. 35, no. 2, pp. 529–535, 2019.
- [27] J. Llobera and C. Charbonnier, "Physics-based character animation and human motor control," *Physics of Life Reviews*, vol. 46, pp. 190–219, 2023. [Online]. Available: <https://www.sciencedirect.com/science/article/pii/S1571064523000775>
- [28] J. Merel, M. Botvinick, and G. Wayne, "Hierarchical motor control in mammals and machines," *Nature communications*, vol. 10, no. 1, p. 5489, 2019.
- [29] R. Leiras, J. M. Cregg, and O. Kiehn, "Brainstem circuits for locomotion," *Annual Review of Neuroscience*, vol. 45, no. Volume 45, 2022, pp. 63–85, 2022. [Online]. Available: <https://www.annualreviews.org/content/journals/10.1146/annurev-neuro-082321-025137>
- [30] W. Maish. (2019) The ascending tracts of the central nervous system. [Online]. Available: <https://geekymedics.com/the-ascending-tracts-of-the-central-nervous-system/>
- [31] A. L. Hodgkin and A. F. Huxley, "A quantitative description of membrane current and its application to conduction and excitation in nerve," *The Journal of physiology*, vol. 117, no. 4, p. 500, 1952.
- [32] A. N. Burkitt, "A review of the integrate-and-fire neuron model: I. homogeneous synaptic input," *Biological cybernetics*, vol. 95, pp. 1–19, 2006.
- [33] R. B. Stein, "A theoretical analysis of neuronal variability," *Biophysical journal*, vol. 5, no. 2, pp. 173–194, 1965.
- [34] E. O. Neftci, H. Mostafa, and F. Zenke, "Surrogate gradient learning in spiking neural networks: Bringing the power of gradient-based optimization to spiking neural networks," *IEEE Signal Processing Magazine*, vol. 36, no. 6, pp. 51–63, 2019.
- [35] A. Henkes, J. K. Eshraghian, and H. Wessels, "Spiking neural networks for nonlinear regression," *Royal Society Open Science*, vol. 11, no. 5, p. 231606, 2024.
- [36] C. Urrea, Y. Garcia-Garcia, and J. Kern, "Closed-form continuous-time neural networks for sliding mode control with neural gravity compensation," *Robotics*, vol. 13, no. 9, 2024. [Online]. Available: <https://www.mdpi.com/2218-6581/13/9/126>
- [37] A. P. Georgopoulos, A. B. Schwartz, and R. E. Kettner, "Neuronal population coding of movement direction," *Science*, vol. 233, no. 4771, pp. 1416–1419, 1986.
- [38] W. Gerstner and W. M. Kistler, *Spiking neuron models: Single neurons, populations, plasticity*. Cambridge university press, 2002.
- [39] A. Paszke, S. Gross, F. Massa, A. Lerer, J. Bradbury, G. Chanan, T. Killeen, Z. Lin, N. Gimelshein, L. Antiga *et al.*, "Pytorch: An imperative style, high-performance deep learning library," *Advances in neural information processing systems*, vol. 32, 2019.
- [40] W. Fang, Y. Chen, J. Ding, Z. Yu, T. Masquelier, D. Chen, L. Huang, H. Zhou, G. Li, and Y. Tian, "Spikingjelly: An open-source machine learning infrastructure platform for spike-based intelligence," *Science Advances*, vol. 9, no. 40, p. eadi1480, 2023. [Online]. Available: <https://www.science.org/doi/abs/10.1126/sciadv.adi1480>
- [41] E. Coumans and Y. Bai, "Pybullet, a python module for physics simulation for games, robotics and machine learning," <http://pybullet.org>, 2016–2021.
- [42] D. Bennett, J. Hollerbach, Y. Xu, and I. Hunter, "Time-varying stiffness of human elbow joint during cyclic voluntary movement," *Experimental brain research*, vol. 88, pp. 433–442, 1992.
- [43] T. D. Sanger, "Human arm movements described by a low-dimensional superposition of principal components," *Journal of Neuroscience*, vol. 20, no. 3, pp. 1066–1072, 2000.
- [44] C. J. Forgaard, I. M. Franks, D. Maslovat, L. Chin, and R. Chua, "Voluntary reaction time and long-latency reflex modulation," *Journal of neurophysiology*, vol. 114, no. 6, pp. 3386–3399, 2015.

**Yanbo Pang** received the B.Eng. from Sun Yat-sen University in 2022 and the M.Sc. from Tsinghua University in 2025. He is currently an intern at Booster Robotics. His research interests include neuromorphic computing, neurorobotics and robotic arm control.

**Qingkai Li** received his B.S. from Tsinghua University in 2021. He is currently a Ph.D. candidate in the Department of Automation at Tsinghua University, with research interests spanning neuromorphic computing, bio-inspired algorithms, imitation learning, and whole-body control.

**Mingguo Zhao** received the B.Eng., M.Sc. and Ph.D. from Harbin Institute of Technology in 1995, 1997 and 2001, respectively. He is currently a Full Professor with the Department of Automation and a director of the Beijing Innovation Center for Future Chips, Tsinghua University. His research interests include brain-inspired robot control and general robotic platform based on neuromorphic computing and hardware.